Proceedings of the 26th International Conference on Pattern Recognition (ICPR 2022), Montréal, Québec, Canada, 21–25 August 2022, pp. 421–427. — Original version at https://ieeexplore.ieee.org

Towards Quality Assessment of Blind Deconvolution with Shift Compensation

Ghada Laribi* and Martin Welk†
UMIT – Private University for Health Sciences, Medical Informatics and Technology
Eduard-Wallnöfer-Zentrum 1, 6060 Hall/Tyrol, Austria
Email: *ghada.laribi@umit-tirol.at, †martin.welk@umit-tirol.at

***Abstract*—Quantitative assessment of restoration quality in blind deconvolution is not straightforward. The intricacy comes from the opposite shifts occurring during image reconstruction in both the reconstructed image and point-spread function. State of the art procedures attempting alignment lack specificity and might actually induce interpolation-based errors, whereas alignment-free approaches disregard the possibility of shift variability. Other methods introduce a superresolution-based MSE/PSNR measure involving non-integer shifts. We propose a method to estimate non-integer displacements between the ground-truth image and the reconstructed image via the Fourier domain, which enables at the same time to incorporate interpolation-free shift compensation into the computation of MSE/PSNR measures. We tested our method on synthetically shifted images with additive noise as well as deconvolution results with known shift. Results indicate that distortions of error measures are reduced compared to interpolation-based shift compensation methods, getting closer to a fair assessment of restoration quality without wrongly favouring any blind deconvolution method over another. It was observed that PSNR measures corrected with estimated displacements are close to those corrected with real displacements.**

***Keywords*—** blind image deblurring, image quality assessment, restoration quality, shift estimation, Fourier method

I. Introduction

Deblurring images without prior knowledge about the blur kernel is a recurrent problem for which a great variety of blind deconvolution approaches have been investigated in the last decades [2], [3], [4], [5], [6], [7], [8], [9], [10], [11], [13], [16], [17], [22]. This creates the need for reliable ways to assess and compare the restoration quality achieved by different blind deconvolution methods. Besides visual assessment, quantitative measures are highly demanded.

Assuming that the blur is spatially invariant, a common model of the blurring process is a convolution between the unobserved sharp image g and the point-spread function (PSF) h with additive noise n. The observed blurred image f is then given by $f = g * h + n$.

Methods that aim at recovering the original sharp image from the blur model are called deconvolution. We distinguish two types of deconvolution problems: non-blind deconvolution assuming the blurred image f and the PSF h are known and u (an approximation of g) should be estimated. However, the knowledge of h is often not available in practice, thus one requires blind deconvolution methods where both u and h are to be estimated.

Restoration quality of non-blind deconvolution is often quantified by pointwise error measures such as mean square error MSE or average absolute error AAE as well as further measures derived from MSE such as signal-to-noise ratio SNR and peak signal-to-noise ratio PSNR. Another measure which is claimed to put more emphasis on significant structural details like edges is the structural similarity index (SSIM) [18].

Given a reference (ground-truth) image g and reconstructed image u each of size $n \times m$ pixels, their MSE and PSNR are given by

$$\mathrm{MSE}(g,u) = \frac{1}{nm}\sum_{i=0}^{n-1}\sum_{j=0}^{m-1}(g_{i,j}-u_{i,j})^2\,, \tag{1}$$

$$\mathrm{PSNR}(g,u) = 10\,\log_{10}\,\frac{R(g)^2}{\mathrm{var}(g-u)}\mathrm{dB}\,. \tag{2}$$

Herein, the range R(g) and variance var(g) are given by

$$R(g) = \max_{i,j} g_{i,j} - \min_{i,j} g_{i,j}\,, \tag{3}$$

$$\mathrm{var}(g) = \frac{1}{nm}\sum_{i=0}^{n-1}\sum_{j=0}^{m-1}\big(g_{i,j}-\mu(g)\big)^2 \tag{4}$$

where $\mu(g)$ is the mean intensity of g. If $\mu(u) = \mu(g)$, one has

$$\mathrm{PSNR}(g,u) = 10\,\log_{10}\,\frac{R(g)^2}{\mathrm{MSE}(g,u)}\mathrm{dB}\,. \tag{5}$$

Although these measures are the best established standard we have so far for non-blind deconvolution, they are still limited and do often not capture the visual quality of deblurred images very well.

Unfortunately, quality measurement for blind deconvolution suffers from an additional complication: In blind deconvolution, the restoration of image u and PSF h is only up to opposite but otherwise unknown shifts. Thus, pointwise comparison methods such as MSE, AAE, PSNR do not yield valid results unless combined with additional steps to account for those displacements, i.e. some kind of rigid registration restricted to translations.

If we assume u to be the reconstructed image of a ground-truth image g using a blind deconvolution method, then u can possibly be shifted by an arbitrary, often non-integer displacement $\boldsymbol{d}$, where the recovered point-spread function h_u is translated by $-\boldsymbol{d}$. By means of convolution, these translations cancel each other, i.e. $u * h_u$ is almost equivalent to $g * h$, if we ignore the additive noise. In Figure 1, we show an example of such shifts in blind deconvolution results.

This means that any two blind deconvolution results that differ just by opposite shifts of u and h must be considered equally valid. Consequently, point-wise quality comparison methods MSE/PSNR are precluded without prior adjustment.

Nonetheless, we witness through blind deconvolution literature instances of PSNR-based comparison as well as other standard quantitative measures without any alignment, e.g. [6], [7], [8], [9], [10]. This can be valid only under the assumption that the recovered PSF is aligned with the ground-truth PSF. Other studies showed shift compensation efforts [7], [16], [21].

In [7] where superposition of copies of a sharp image shifted along a curve is used to simulate camera-shake blur, it is proposed to avoid alignment steps by constraining shifts to the camera-shake curve. Restoration results are then compared against the translated ground-truth images used in generating the synthetically blurred image, and

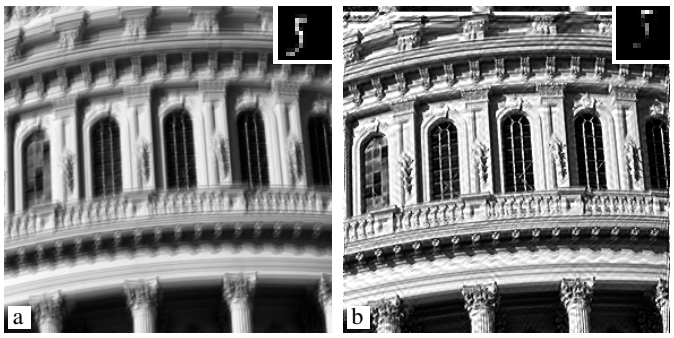

Fig. 1: **(a)** Synthetically blurred image with ground-truth PSF, from [11]. – **(b)** Blind deconvolution result with PSF, from [13]. Note the opposite shifts of image and PSF.

the best match is used for the error measure. This, however, appears to be an overly restrictive assumption since there is no reason for blind deconvolution to yield only shifts that match the trajectory generating the ground-truth PSF.

To measure absolute errors of the particularly aligned blur estimate with regard to the ground truth, the work [16] based on [7] and data from [9] takes into consideration unconstrained displacements, although alignment details were not provided.

Specifying the alignment procedure comes with some choices to make: which interpolation method to use in the registration process? Should we register the reconstructed image to the ground truth or vice versa? The work [20] evaluates the errors introduced by interpolation-based alignment procedures with bilinear and bicubic interpolation. It is demonstrated there that depending on the details chosen during the alignment procedure, the PSNR measures can vary by $1.5\,\mathrm{dB}$ and more. This is a fairly significant amount of uncertainty given that in deconvolution literature often PSNR improvements of as little as $0.5\,\mathrm{dB}$ are considered evidence of superiority of one method over another, compare also [7], [16]. Comparisons of blind deconvolution methods should therefore not be based on such procedures. As an attempt to overcome these difficulties, [20] proposed a superresolution-based error measurement procedure that can significantly reduce the above mentioned alignment-induced variations in MSE/PSNR values. This yields error margins closer to shift-free cases.

In a recent work [14], efforts were directed to measuring the PSF reconstruction quality without the need to refer to a ground-truth. They proposed to utilise inter-row and inter-column correlation coefficients of the restored image to measure the quality of the estimate. Using an iterative modified Richardson-Lucy-based restoration [12], [15] algorithm, they refine the PSF estimate until convergence is reached. The correlation measure is given by the absolute difference between the rates of change of the inter-row and inter-column correlation coefficients. If the required number of iterations is reached, then the absolute difference almost stops changing, under the condition that the blur kernel parameters are set properly.

We are inspired by the same problematic as in [20], while focusing on a scenario where the ground-truth image and the point-spread function are available, and image restoration quality involves measuring the error between the ground-truth and the deblurred image.

So, we aim in this paper to establish a shift estimation procedure between the original image and the reconstructed image from a blind deconvolution procedure.

This will allow us to use the standard quality assessment measures like MSE/PSNR along with the correction of the displacement, thus avoiding aligning induced errors, and forceful assumptions about the trajectory of both reconstructed PSFs and ground truth.

Structure of the paper. In section II we will present our shift estimation procedure, as well as the formulation steps. In section III, we evaluate our approach by running several series of experiments on synthetically shifted image test cases and non-blind deconvolution-based synthetic test cases as well, then we observe and interpret the available results. Section IV includes a conclusion and summary revolving around our experiments, observations and future aspirations.

II. Formulation of the shift estimation

We consider g and h to be the ground-truth image and PSF, and u and h to be respectively the recovered versions of g and h using blind deconvolution. We regard v and h_v to be different potential approximates from the latter using the same blind deconvolution method. Here, v and h_v might be translated by arbitrary non-integer opposite shifts $\boldsymbol{\Delta x}$ and $-\boldsymbol{\Delta x}$ as shown in

$$v(\boldsymbol{x}) = u(\boldsymbol{x} + \boldsymbol{\Delta x})\,, \qquad h_v(\boldsymbol{x}) = h(\boldsymbol{x} - \boldsymbol{\Delta x}) \tag{6}$$

$$f(\boldsymbol{x}) = (u * h)(\boldsymbol{x}) = (v * h_v)(\boldsymbol{x}) \tag{7}$$

Due to the Rayleigh/Parseval equality

$$\int |\hat{u}|^2 \,\mathrm{d}\boldsymbol{\omega} = \int |u|^2 \,\mathrm{d}\boldsymbol{x}\,, \tag{8}$$

both displacement estimation and its compensation can be done in the Fourier domain, which even simplifies computations. In fact,

$$\hat{v}(\boldsymbol{\omega}) = \hat{u}(\boldsymbol{\omega})\mathrm{e}^{-\mathrm{i}\langle\boldsymbol{\omega},\boldsymbol{\Delta x}\rangle}\,, \qquad \hat{h_v}(\boldsymbol{\omega}) = \hat{h}(\boldsymbol{\omega})\mathrm{e}^{+\mathrm{i}\langle\boldsymbol{\omega},\boldsymbol{\Delta x}\rangle}\,, \tag{9}$$

$$\hat{f}(\boldsymbol{\omega}) = \hat{u}(\boldsymbol{\omega})\hat{h}(\boldsymbol{\omega}) = \hat{v}(\boldsymbol{\omega})\hat{h_v}(\boldsymbol{\omega})\,. \tag{10}$$

This conveys that one must not punish a blind deconvolution method for wrongly guessing the position. In other words, blind deconvolution results that differ just by such opposite translations of u and h must be considered equally valid reconstructions.

In order to overcome these limits in quality measurement, we propose to estimate the displacement $\boldsymbol{\Delta x}$ by considering the phase discrepancy $\varphi(\boldsymbol{\omega})$ between $\hat{u}$ and $\hat{v}$, which is given by

$$\frac{\hat{v}(\boldsymbol{\omega})}{\hat{u}(\boldsymbol{\omega})} = \mathrm{e}^{-\mathrm{i}\varphi(\boldsymbol{\omega})}\,, \qquad \varphi(\boldsymbol{\omega}) = \arg\left(\frac{\hat{v}(\boldsymbol{\omega})}{\hat{u}(\boldsymbol{\omega})}\right)\,. \tag{11}$$

where arg denotes the angular coordinate of a complex number in polar representation. Motivated by (9), we aim at fitting a linear function $\langle\boldsymbol{\omega},\boldsymbol{\Delta x}\rangle$ to φ to obtain $\boldsymbol{\Delta x}$. Then we can correct the displacement along with measuring the MSE and/or PSNR between the ground truth u and the blind deconvolution result v via

$$\int \big(u(\boldsymbol{x}) - v(\boldsymbol{x} - \boldsymbol{\Delta x})\big)^2 \mathrm{d}\boldsymbol{x} = \int \big|\hat{u}(\boldsymbol{\omega}) - \hat{v}(\boldsymbol{\omega})\mathrm{e}^{+\mathrm{i}\langle\boldsymbol{\omega},\boldsymbol{\Delta x}\rangle}\big|^2 \mathrm{d}\boldsymbol{\omega}\,. \tag{12}$$

For the linear function fit, we could in principle minimise

$$\sum \big(\varphi(\boldsymbol{\omega}) - \langle\boldsymbol{\omega},\boldsymbol{\Delta x}\rangle\big)^2\,. \tag{13}$$

This is, however, insufficient as we have so far ignored the wrap-around nature of phase factors of high frequencies. Therefore, we weight contributions of different frequencies with a Gaussian function of the frequency $\lambda(\boldsymbol{\omega})$. Initially the standard deviation is chosen to be very small such that the fitting is essentially restricted to frequencies close to the center for which no wrap-around is expected to take place. Our energy function therefore reads

$$\sum \lambda(\boldsymbol{\omega})\big(\varphi(\boldsymbol{\omega}) - \langle\boldsymbol{\omega},\boldsymbol{\Delta x}\rangle\big)^2\,. \tag{14}$$

Using the notations $\boldsymbol{\Delta x} = (\Delta x, \Delta y)^{\mathrm{T}}$, $\boldsymbol{\omega} = (\xi, \eta)^{\mathrm{T}}$ we take derivatives of (14) with regard to Δx and Δy. Equating these to zero yields a system of two linear equations for Δx and Δy:

$$\sum \lambda(\boldsymbol{\omega})\xi^2\Delta x + \sum \lambda(\boldsymbol{\omega})\xi\eta\Delta y = \sum \lambda(\boldsymbol{\omega})\varphi(\boldsymbol{\omega})\xi\,, \tag{15}$$

$$\sum \lambda(\boldsymbol{\omega})\xi\eta\Delta x + \sum \lambda(\boldsymbol{\omega})\eta^2\Delta y = \sum \lambda(\boldsymbol{\omega})\varphi(\boldsymbol{\omega})\eta\,. \tag{16}$$

Proceeding further, we must take into account the wrap-around of the phase in the frequency domain. Given the estimate $\boldsymbol{\Delta x}$, phase unwrapping means to detect the discontinuities (2π jumps) in the phase spectrum of $\varphi(\boldsymbol{\omega})$, i.e. to determine the integer multiples of 2π in agreement with the discontinuities at each frequency, and to add them to the phase values $\varphi(\boldsymbol{\omega})$ at each frequency $\boldsymbol{\omega}$.

Samples $\varphi(\boldsymbol{\omega})$ should in fact be close to $\langle \boldsymbol{\omega}, \boldsymbol{\Delta x} \rangle$ or off by multiples of 2π, thus we iteratively updated Δx and Δy estimates in order to correct $\varphi(\boldsymbol{\omega})$ and refine the estimation results.

In each iteration, we compute a residual phase function

$$\varphi_{\mathrm{res}}(\boldsymbol{\omega}) = (\varphi(\boldsymbol{\omega}) - 2\pi\langle \boldsymbol{\omega}, \boldsymbol{\Delta x} \rangle) \bmod_{\pm} 2\pi \tag{17}$$

where $\bmod_{\pm} 2\pi$ indicates modulo-2π reduction to the interval $[-\pi, +\pi)$. An incremental update for $\boldsymbol{\Delta x}$ is then computed by solving (15)–(16) with $\varphi_{\mathrm{res}}(\boldsymbol{\omega})$ instead of $\varphi(\boldsymbol{\omega})$.

During the iterative refinement, the standard deviation of the Gaussian weight function is successively increased so the contributions of higher frequencies are gradually included in the refinement procedure.

In order to reduce the impact of generated boundary artifacts due to the blind deconvolution process on the shift estimation, we preprocess both the original image and its deblurred version by excluding boundary adjacent areas using a trim-window in both directions x and y of the image

$$S_{T_1,T_2}(i,n) = \begin{cases} 0, & i \le T_1 \text{ or } i \ge n-1-T_1 \\ 1, & T_2 \le i \le n-1-T_2 \\ \frac{2(i-T_1)^2}{(T_2-T_1)^2}, & T_1 < i \le \frac{T_1+T_2}{2} \\ 1 - \frac{2(T_2-i)^2}{(T_2-T_1)^2}, & \frac{T_1+T_2}{2} < i < T_2 \\ \frac{2(n-1-T_1-i)^2}{(T_2-T_1)^2}, & T_1 \le n-1-i \le \frac{T_1+T_2}{2} \\ \frac{2(i-n+1-T_2)^2}{(T_2-T_1)^2}, & \frac{T_1+T_2}{2} \le n-1-i \le T_2 \end{cases} \tag{18}$$

where T_1 and T_2 are the window delimiters, with $0 < T_1 < T_2$, n is the size of the image in x or y direction and i is the pixel position. The piecewise quadratic function S_{T_1,T_2} suppresses a region of width T_1 at the image boundaries. Within a wider margin of width T_2, it ensures a smooth transition to the unattenuated centre part of the image. The smooth transition is chosen such as not to create spurious sharp edges that would misguide the displacement estimation.

III. Experiments on synthetic data

1) Test cases with synthetic shifts: To test our approach for shift estimation and correction we start by generating a fully synthetic set of shifted images with various choices for the original image, additive noise, additional boundary artifacts, and interpolation method (bilinear, bicubic).

Since common displacements in blind deconvolution results usually do not exceed a 2 pixels limit (or larger displacements can be reduced to this range by compensating their integer part with interpolation-free block-moving of pixels), we focus on 20 random values of the shift in the interval $[0, 2]$. To complement the picture, we include a few more samples with larger shifts up to 10. Besides the value of the displacement, test case generation as mentioned above has four more inputs: the interpolation method, the choice of padding, the noise, and the boundary artifacts, if added. To generate the test cases we employ bilinear and bicubic interpolation with zero-padding and Gaussian noise ($\sigma = 20$) and as well as increased Gaussian noise ($\sigma = 40$) around the boundary to simulate boundary artifacts as they are common in deconvolution results, see e.g. Figure 3 (d) later in this paper. An example with bicubic interpolation is shown in Figure 2.

We use then our shift estimation approach to retrieve an approximation of the shift vector $\boldsymbol{\Delta x}$ for each image generated. In the shift estimation it is important to suppress the influence of the boundary region where large errors due to boundary conditions and boundary artifacts are observed. To this end we apply the trim-window (18) with $T_1 = 20$ and $T_2 = 45$. However, applying the trim-window to both the ground-truth and the shifted image in their original coordinates introduces larger areas of mismatch along the window boundaries, thus larger error contributions. Therefore we modify the windowing procedure by using the initial estimate of the shift to adjust the placement of the windowing function on both images. In particular, We shift the window in (18) by $\boldsymbol{\Delta x}/2$ for the original image, and $-\boldsymbol{\Delta x}/2$ for its shifted version. We call the modified trim-window adaptive window.

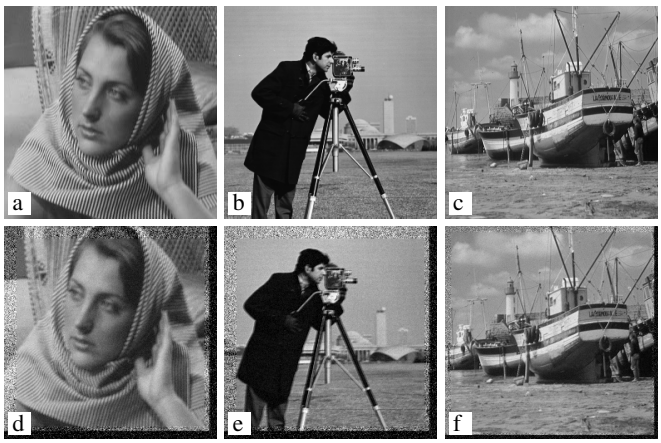

Fig. 2: **(a–c)** Clippings of *Barbara*, *Camera* and *Boat* images. – **(d–f)** Same images shifted by -9.75 in x direction and -9.75 in y direction with zero-padding, Gaussian additive noise ($\sigma = 20$) and simulated boundary artifacts ($\sigma = 40$).

An initial prediction of the shift prior to applying the adapted window tends to improve the MSE/PSNR values along with the new estimate, if used to adjust the window from (18). We then experiment with iterating the shift estimation (Algorithm 1) and adaptive windowing (Algorithm 2) as depicted in Algorithm 3 and observe that at about 3 iterations the results become stationary, hence the choice of the number of iterations 3. Note that n_x and n_y are image sizes in x and y direction, respectively.

We tested as well a slightly modified variant of the overall estimation procedure. We added another step prior to the iterative windowing and estimation method (Algorithm 3), where we estimate the shift and use its integer part for shift compensation. In other words, we correct the integer displacement of the shifted image by means of translation, see Algorithm 4, then we proceed to apply the iterative windowing and estimation procedure between the original image and the corrected shifted image. This leaves us with only the fractional remaining displacement to estimate. We observe that this

Algorithm 1 Shift estimation function

Input: Original image $u(n_x, n_y)$, shifted image $v(n_x, n_y)$
Output: $\boldsymbol{\Delta x}$

Initialise $\boldsymbol{\Delta x} = 0$
Apply 2D Fourier transform to u and v
Compute $\varphi(\boldsymbol{\omega})$ from $\hat{u}$ and $\hat{v}$ using (11)
Shift estimation :
for $i = 0$ to 10 **do**
  Compute $\lambda(\boldsymbol{\omega})$
  Update $\boldsymbol{\Delta x}$ by solving (15), (16)
end for
return $\boldsymbol{\Delta x}$

additional step from Algorithm 4 leads to measurable improvement, especially when it comes to shifts larger than 1.

To experiment with multiple instances of the same image with a single shift and random noise, we create 10 instances of each test case with identical parameters (shift, interpolation method, boundary conditions, noise standard deviation, boundary artifacts) but different random noise instantiation.

In Table I and Table II we display exemplary results for shifts performed with bilinear and bicubic interpolation. For each shift and test image, PSNR, Δx and Δy as reported in the tables are averages of the values from the 10 random runs with the same parameters.

Algorithm 2 Windowing procedure

Input: Original image $u(n_x, n_y)$, shifted image $v(n_x, n_y)$, T_1, T_2 and $\boldsymbol{\Delta x}$
Output: Windowed original image u_{wd}, windowed shifted image v_{wd}

Initialise $u_{\mathrm{wd}}(n_x, n_y)$, $v_{\mathrm{wd}}(n_x, n_y)$
Windowing process:
for $i = 0$ to n_x **do**
  for $j = 0$ to n_y **do**
    Compute $u_{\mathrm{wd}}(i,j) = u(i,j) S_{T_1,T_2}(i + \Delta x/2, n_x) \times S_{T_1,T_2}(j + \Delta y/2, n_y)$ using (18)
    Compute $v_{\mathrm{wd}}(i,j) = v(i,j) S_{T_1,T_2}(i - \Delta x/2, n_x) \times S_{T_1,T_2}(j - \Delta y/2, n_y)$ using (18)
  end for
end for
return u_{wd} and v_{wd}

Algorithm 3 Iterative windowing and estimation procedure

Input: Original image $u(n_x, n_y)$, shifted image $v(n_x, n_y)$, T_1, T_2
Output: $\boldsymbol{\Delta x}$, MSE and PSNR

Initialise $\boldsymbol{\Delta x}$
for $i = 0$ to 3 **do**
  Apply adaptive window using Algorithm 2
  Estimate $\boldsymbol{\Delta x}$ using Algorithm 1
  Update $\boldsymbol{\Delta x}$
end for
Measure MSE with displacement correction using (12)
Compute PSNR from MSE using (5)
return $\boldsymbol{\Delta x}$, MSE and PSNR

Algorithm 4 Integer shift compensation

Input: Original image $u(n_x, n_y)$, shifted image $v(n_x, n_y)$
Output: Corrected shifted image $v_c(n_x, n_y)$

Initialise $\boldsymbol{\Delta x} = 0$, $\boldsymbol{\Delta}_{\mathbf{int}}\boldsymbol{x} = 0$ and $v_c(n_x, n_y)$
Estimate $\boldsymbol{\Delta x}$ using Algorithm 1
Compute $\Delta_{\mathrm{int}} x = \lfloor \Delta x + 0.5 \rfloor$, $\Delta_{\mathrm{int}} y = \lfloor \Delta y + 0.5 \rfloor$
for $i = 0$ to $n_x - \Delta_{\mathrm{int}} x$ **do**
  for $j = 0$ to $n_y - \Delta_{\mathrm{int}} y$ **do**
    Compute $v_c(i,j) = v(i + \Delta_{\mathrm{int}} x, j + \Delta_{\mathrm{int}} y)$
  end for
end for
return $v_c(n_x, n_y)$

We present in Table I and Table II, respectively, the results yielded by applying the first (Algorithm 3) and second (Algorithm 4 and Algorithm 3) variants of the estimation procedure. Note that the variables in Table II carry an additional "c" subscript indicating the compensation of integer shifts by Algorithm 4. Let us further detail the variables used in Table I and Table II: $\mathrm{PSNR_t}$ and $\mathrm{PSNR_{tc}}$ are the PSNR results if true values of Δx and Δy were used in the windowing process, instead of the previous estimates. They represent the best results we can get, if we cheat in the windowing process. $\mathrm{PSNR_3}$ (resp. $\mathrm{PSNR_{3c}}$), $\Delta_3 x$ (resp. $\Delta_{3\mathrm{c}} x$) and $\Delta_3 y$ (resp. $\Delta_{3\mathrm{c}} y$) are the third iteration results.

We proceed to compare $\mathrm{PSNR_3}$ (resp. $\mathrm{PSNR_{3c}}$) values to the reference $\mathrm{PSNR_t}$ (resp. $\mathrm{PSNR_{tc}}$), and $\Delta_3 x$ (resp. $\Delta_{3\mathrm{c}} x$) and $\Delta_3 y$ (resp. $\Delta_{3\mathrm{c}} y$) to the true values of Δx and Δy. Note that we used $T_1 = 20$ and $T_2 = 45$ in our windowing process.

We observe that for small shifts, $|\Delta x|, |\Delta y| < 1$, both variants of the proposed shift estimation procedure behave almost identically which is expected because the integer part of these shifts is 0. We notice that the differences $(|\mathrm{PSNR_3} - \mathrm{PSNR_t}|)$ (resp. $(|\mathrm{PSNR_{3c}} - \mathrm{PSNR_{tc}}|)$) do not exceed 0.5 dB when it comes to bilinear interpolation test cases where $|\Delta x|, |\Delta y| < 2$. This is a very important observation, since often superiority of one blind

TABLE I: Shift estimation and quality assessment PSNR results from Algorithm 3

$(\Delta x, \Delta y)$	Image	$\mathrm{PSNR_3}$	$\mathrm{PSNR_t}$	$\Delta_3 x$	$\Delta_3 y$
Bilinear Interpolation					
$(-0.125, -0.25)$	Barbara	32.1395	31.8633	-0.100	-0.216
	Cameraman	31.8314	31.6190	-0.099	-0.216
	Boat	33.2252	33.1883	-0.118	-0.239
$(-0.333, -0.879)$	Barbara	29.3757	29.2398	-0.300	-0.875
	Cameraman	30.3220	30.1983	-0.300	-0.885
	Boat	31.9868	31.9601	-0.323	-0.872
$(-0.5, -0.5)$	Barbara	28.1160	28.1224	-0.489	-0.489
	Cameraman	28.6100	28.6140	-0.489	-0.490
	Boat	31.2281	31.2297	-0.493	-0.492
$(-1.75, -0.4)$	Barbara	29.6592	29.6837	-1.750	-0.380
	Cameraman	29.7614	29.7339	-1.752	-0.375
	Boat	32.0108	32.0914	-1.731	-0.392
$(-9.3, -8.25)$	Barbara	26.1328	29.1226	-8.993	-7.944
	Cameraman	27.3287	29.7921	-9.000	-7.974
	Boat	31.8375	31.9687	-9.159	-8.123
$(-7.89, -9.3)$	Barbara	25.8910	32.5645	-7.666	-8.952
	Cameraman	27.7239	31.4007	-7.695	-9.013
	Boat	32.1943	33.2129	-7.782	-9.1587
Bicubic Interpolation					
$(-0.125, -0.25)$	Barbara	33.8990	33.3827	-0.097	-0.218
	Cameraman	33.4158	33.0222	-0.100	-0.214
	Boat	33.8225	33.7564	-0.115	-0.241
$(-0.333, -0.879)$	Barbara	31.8278	30.5615	-0.223	-0.878
	Cameraman	32.2144	31.0294	-0.244	-0.887
	Boat	33.0585	32.3990	-0.233	-0.872
$(-0.5, -0.5)$	Barbara	30.4804	30.4668	-0.455	-0.486
	Cameraman	30.2610	30.2275	-0.454	-0.488
	Boat	32.0865	32.0871	-0.438	-0.490
$(-1.75, -0.4)$	Barbara	30.6803	31.3548	-1.705	-0.359
	Cameraman	30.7272	30.9268	-1.708	-0.357
	Boat	31.8863	32.6319	-1.645	-0.386
$(-9.3, -8.25)$	Barbara	26.6331	31.6411	-8.998	-7.951
	Cameraman	28.0663	31.6509	-9.005	-7.980
	Boat	32.8439	32.9200	-9.158	-8.124
$(-7.89, -9.3)$	Barbara	25.9627	33.1208	-7.672	-8.972
	Cameraman	27.6577	32.4346	-7.671	-8.995
	Boat	31.7654	33.5790	-7.724	-9.155

deconvolution methods over another is claimed based on as little as $0.5\,\mathrm{dB}$ of improvement in literature [7], [16]. However, we witness rare cases of a moderately larger margin up to 1.2676 for bicubic interpolation-based data. In some cases, PSNR_3 (resp. $\mathrm{PSNR}_{3\mathrm{c}}$) values slightly exceed PSNR_t (resp. $\mathrm{PSNR}_{\mathrm{tc}}$). This is most probably caused by the influence of the noise especially when the shift is small. Moreover, when it comes to slightly larger shifts (1 up to 2), we observe the first manifestations of a rather larger gap between PSNR_3 and $\mathrm{PSNR}_{3\mathrm{c}}$. For even larger shifts like $(-7.89, -9.3)$ in Table I and Table II, e.g. for the Barbara image, the PSNR_3 value reaches a low $25.9627\,\mathrm{dB}$, furthermore, the differences $(\mathrm{PSNR}_3 - \mathrm{PSNR}_\mathrm{t})$ stretch to as much as $7.1581\,\mathrm{dB}$. Meanwhile, $\mathrm{PSNR}_{3\mathrm{c}}$ is a healthy $32.6542\,\mathrm{dB}$ with $(\mathrm{PSNR}_{3\mathrm{c}} - \mathrm{PSNR}_{\mathrm{tc}}) = 0.28\,\mathrm{dB}$.

These results demonstrate that the second variant of the proposed shifted estimation procedure outperforms the first one. Besides, we notice for the second algorithm variant results in Table II, whether the shift is small or large, that $(\mathrm{PSNR}_{3\mathrm{c}} - \mathrm{PSNR}_{\mathrm{tc}})$ is below $0.5\,\mathrm{dB}$ almost consistently for bilinear interpolation-based data while it exceeds $1\,\mathrm{dB}$ for bicubic interpolation-based data in rare cases. These outcomes are still faithful to our purpose: a fair quality assessment between two given blind deconvolution methods.

TABLE II: Shift estimation and quality assessment PSNR results after integer shift compensation 4

$(\Delta x,\, \Delta y)$	Image	$\mathrm{PSNR}_{3\mathrm{c}}$	$\mathrm{PSNR}_{\mathrm{tc}}$	$\Delta_{3\mathrm{c}}x$	$\Delta_{3\mathrm{c}}y$
Bilinear Interpolation					
$(-0.125, -0.25)$	Barbara	32.1765	32.1395	-0.100	-0.216
	Cameraman	31.8314	31.6160	-0.099	-0.216
	Boat	33.2252	33.1883	-0.118	-0.239
$(-0.333, -0.879)$	Barbara	29.3717	29.2452	-0.299	-0.900
	Cameraman	30.3421	30.2066	-0.300	-0.900
	Boat	31.9931	31.9592	-0.323	-0.885
$(-0.5, -0.5)$	Barbara	28.1160	28.1220	-0.489	-0.489
	Cameraman	28.6100	28.6184	-0.489	-0.498
	Boat	31.2272	31.2282	-0.505	-0.498
$(-1.75, -0.4)$	Barbara	29.8718	29.6998	-1.780	-0.375
	Cameraman	29.8780	29.7316	-1.785	-0.374
	Boat	32.1283	32.0897	-1.759	-0.392
$(-9.3, -8.25)$	Barbara	29.4723	29.2704	-9.266	-8.218
	Cameraman	29.8178	29.8442	-9.266	-8.214
	Boat	31.9808	31.9550	-9.290	-8.241
$(-7.89, -9.3)$	Barbara	32.1744	32.2020	-7.913	-9.269
	Cameraman	31.3882	31.4680	-7.914	-9.268
	Boat	33.2178	33.2055	-7.897	-9.287
Bicubic Interpolation					
$(-0.125, -0.25)$	Barbara	33.8990	33.3827	-0.097	-0.218
	Cameraman	33.4158	33.0222	-0.100	-0.214
	Boat	33.8225	33.7564	-0.115	-0.241
$(-0.333, -0.879)$	Barbara	31.8309	30.5633	-0.222	-0.898
	Cameraman	32.2646	31.0368	-0.223	-0.904
	Boat	33.0750	32.3981	-0.232	-0.887
$(-0.5, -0.5)$	Barbara	30.4804	30.4668	-0.455	-0.486
	Cameraman	30.2601	30.2315	-0.453	-0.495
	Boat	32.0861	32.0870	-0.438	-0.492
$(-1.75, -0.4)$	Barbara	31.1714	31.3744	-1.738	-0.356
	Cameraman	30.9923	30.9243	-1.740	-0.357
	Boat	32.1488	32.6300	-1.674	-0.386
$(-9.3, -8.25)$	Barbara	31.9840	31.7102	-9.2637	-8.213
	Cameraman	31.8275	31.6964	-9.264	-8.215
	Boat	32.9708	32.9051	-9.287	-8.240
$(-7.89, -9.3)$	Barbara	32.8794	33.1594	-7.890	-9.250
	Cameraman	32.4656	32.4855	-7.888	-9.249
	Boat	33.2496	33.5695	-7.840	-9.284

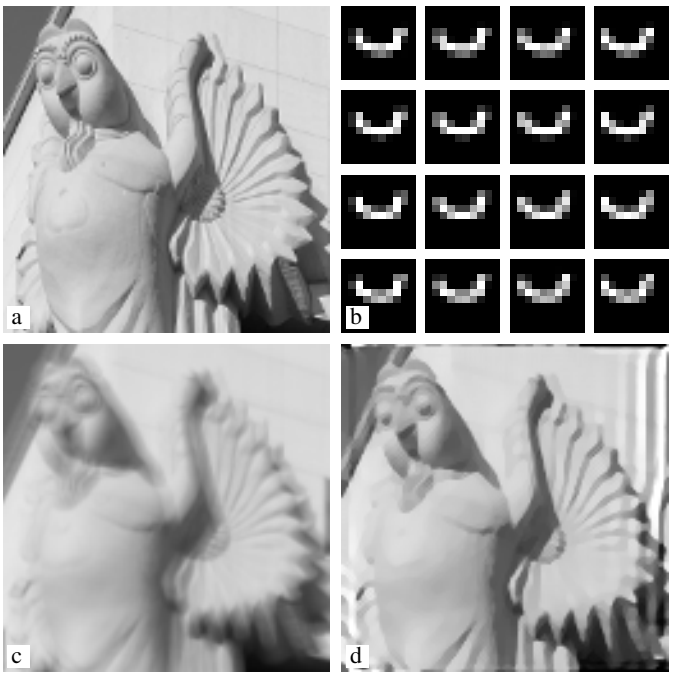

Fig. 3: **(a)** Ground truth image, 128×128 pixels. (Clipped, downscaled and converted to greyscale from a photograph of the building of TU Vienna. Source of original image: https://upload.wikimedia.org/wikipedia/commons/e/e9/TU_Bibl_01_DSC1099w.jpg, Author: Peter Haas. Available under licence CC BY-SA 3.0.) – **(b)** 16 PSFs, 10×10 pixels each, subsampled from the same high-resolution input. The shift from row to row and from column to column is 0.25 pixels. – **(c)** Image (a) blurred by convolution with PSF from (b), first row, second column. – **Bottom right:** Image (c) deblurred with PSF from fourth row, third column, resulting in a shift relative to ground truth of $(0.25, 0.75)$ pixels. This figure is reproduced from [20].

2) Experiments on deconvolution results: To bring the previous procedure closer to a true blind deconvolution context, we experiment with non-blind deconvolution results using data from [20] as displayed in the example Figure 3. In [20], a total of 256 test case images were created based on the ground truth image in Figure 3 (a) by blurring this image with 16 different PSFs shown in Figure 3 (b). All these PSFs are downsampled versions of the same high-resolution PSF with horizontal and vertical shifts in $1/4$ pixel steps. Afterwards, the non-blind deconvolution method from [19] with the same parameters ($\alpha = 0.01$, iterations = 300) was used to deconvolve each of the 16 blurred images, e.g. Figure 3 (c), with each of the 16 PSFs. This yields 256 deblurred images shifted from the ground truth by displacements ranging from -0.75 to 0.75 pixels in x and y direction; Figure 3 (d) is an exemplary deblurred image. We used the same procedure to generate 256 deblurred images from each of the Barbara, camera man and boat images as well. Since we are working with shifts ranging between -0.75 and 0.75, applying and displaying the results of the first variant of the proposed shift estimation method (Algorithm 3) is sufficient for the purpose of this paper. To reduce the impact of boundary artifacts, we apply the trim-window (18) with $T_1 = 20$ and $T_2 = 35$ for the Owl image and $T_1 = 20$ and $T_2 = 40$ for all three of Barbara, Camera man

and Boat images. Table III exhibits some examples from the 256 PNSR and shift values resulting from both our Fourier-based shift estimation method and the superresolution alignment procedure from [20]. It contains the variables $\mathrm{PSNR_t}$, $\mathrm{PSNR_3}$ as well as $\Delta_3 x$ and $\Delta_3 y$, where $\mathrm{PSNR_t}$ represents the PSNR results when true Δx and Δy are used in Algorithm 2, and $\mathrm{PSNR_3}/\boldsymbol{\Delta_3 x}$ are the third iteration results from Algorithm 3. As in the previous experiment, we want to compare $\mathrm{PSNR_t}$ and $\mathrm{PSNR_3}$. We observe in Table III that the differences ($|\mathrm{PSNR_3} - \mathrm{PSNR_t}|$) do not surpass $0.5\,\mathrm{dB}$ for our shift estimation method. As can be expected, the last two columns of Table III indicate, as good as the estimate can get, that there is still room for improvement regarding $\boldsymbol{\Delta x}$ (resp. PNSR) for both methods. The average $\mathrm{PSNR_3}$ value across all 256 test cases for our shift estimation is 30.0639 with a standard deviation of 0.3376 and $40,1981$ for the superresolution alignment procedure with 0.236 as standard deviation. Comparing with the more complicated procedure proposed in [20], it is evident that the variation of the measurement is slightly larger. However, the Fourier-based method described in the present contribution has the advantage that displacement estimation and error measurement are achieved in a joint and fairly efficient procedure.

TABLE III: Shift estimates and quality assessment PSNR results from Algorithm 3 and superresolution alignment [20] using images generated by non-blind deconvolution

$(\Delta x, \Delta y)$	Image	$\mathrm{PSNR_3}$	$\mathrm{PSNR_t}$	$\Delta_3 x$	$\Delta_3 y$
Our Fourier-based shift estimation					
$(0,0)$	Barbara	27.1677	27.1740	0.017	0.000
	Cameraman	32.9230	32.9228	0.001	0.001
	Boat	32.9666	32.9731	−0.008	0.002
	Owl	31.0764	31.0904	−0.015	−0.010
$(0,-0.75)$	Barbara	26.0540	26.0491	0.019	−0.749
	Cameraman	31.3022	31.2928	0.009	−0.748
	Boat	32.2486	32.2270	0.048	−0.755
	Owl	30.2572	30.2431	−0.000	−0.772
$(0.25,0.5)$	Barbara	26.3325	26.3381	0.262	0.491
	Cameraman	30.5055	30.4723	0.235	0.490
	Boat	32.0737	32.0932	0.195	0.486
	Owl	29.9410	29.9805	0.198	0.516
$(-0.25,-0.25)$	Barbara	26.2351	26.2357	−0.249	−0.237
	Cameraman	30.3617	30.3412	−0.246	−0.235
	Boat	32.0330	32.0380	−0.253	−0.233
	Owl	29.8897	29.8687	−0.227	−0.192
$(-0.75,-0.25)$	Barbara	26.5112	26.5138	−0.744	−0.239
	Cameraman	30.8111	30.6877	−0.767	−0.229
	Boat	32.1812	32.2046	−0.735	−0.233
	Owl	30.2255	30.1774	−0.812	−0.174
$(0.75,0.75)$	Barbara	26.7639	26.7480	0.771	0.745
	Cameraman	30.9633	30.7849	0.779	0.752
	Boat	32.3013	32.3470	0.737	0.750
	Owl	30.4082	30.3340	0.786	0.756
Superresolution alignment with innocence assumption as in [20]					
$(0,0)$	Barbara	32.4010	32.4010	0.000	0.000
	Cameraman	38.2900	38.2900	0.000	0.000
	Boat	38.5820	38.5820	0.000	0.000
	Owl	36.0710	36.0710	0.000	0.000
$(0,-0.75)$	Barbara	37.0120	32.1890	0.300	−1.000
	Cameraman	39.3110	39.0820	0.000	−0.700
	Boat	39.3160	39.1680	0.000	−0.700
	Owl	36.8640	36.6930	0.000	−0.700
$(0.25,0.5)$	Barbara	39.4120	37.8420	0.350	0.450
	Cameraman	43.0290	43.0290	0.250	0.500
	Boat	44.3030	43.7340	0.300	0.500
	Owl	40.5940	33.6540	0.300	0.500
$(-0.25,-0.25)$	Barbara	39.0770	37.4580	−0.350	−0.250
	Cameraman	42.3440	41.7680	−0.300	−0.250
	Boat	43.8210	43.0960	−0.300	−0.300
	Owl	40.3910	39.7560	−0.300	−0.300
$(-0.75,-0.25)$	Barbara	39.4530	37.6440	−0.650	−0.350
	Cameraman	42.4840	42.4840	−0.750	−0.250
	Boat	44.0990	43.3570	−0.700	−0.300
	Owl	40.7790	40.0870	−0.700	−0.300
$(0.75,0.75)$	Barbara	39.4500	37.8360	0.650	0.750
	Cameraman	42.7650	42.7650	0.750	0.750
	Boat	44.4280	43.7160	0.700	0.700
	Owl	40.4800	40.3470	0.750	0.700

In contrast, in [20] a costly superresolution procedure was used for error measurement, which was repeated in a brute force grid search for displacement estimation. This procedure is slow and subject to numerous parameters. Even with substantial regularisation, it tends to hide some errors in oscillatory over-fitting artifacts. We experimented with the method in [20] with $\alpha = 0.3$, $\beta = 0.03$ and $\mu = 1$. Remarkably, large differences between $\mathrm{PSNR_t}$ and $\mathrm{PSNR_3}$ again occur for the Barbara example, likely caused by the abundance of higher frequency structures in the image.

We are optimistic that further refinements based on our present contribution will allow to reduce the variation of error measurement depending on the displacement.

IV. Conclusion

In this paper, we established a shift estimation procedure between a ground truth and a shifted image. This shift is then compensated in the MSE measures. As formerly stated in the section I, blind deconvolution restoration of an image u and PSF h is up to unknown non-integer opposite shifts. Therefore, comparison of blind deconvolution methods should not rely on pointwise measures such as MSE or PSNR without performing a prior alignment – rigid registration restricted to translations. The method from section II implements this alignment step in an interpolation-free way which allows further the use of pointwise standard quality assessment measures like MSE/PSNR with blind deconvolution.

Tests on synthetically generated image pairs with known displacements confirmed that shifts could be recovered with good precision and error measurements (PSNR) with the recovered shifts were reasonably close to those obtained with the ground truth displacements.

A further test series was based on test data from [20]. These test cases consisted of non-blind deconvolution results designed to mimic blind deconvolution settings but with full control over the displacements between ground truth and reconstructed images. We also displayed results of experiments with superresolution alignment. We point out that despite the strong overlap in the problem statement with [20], our approach is entirely different. While both methods give decent shift estimates and improved PSNR values, there is a slight improvement with Fourier-based shift estimation when it comes to lesser likelihood to over-fitting errors, and a substantial reduction in parameters. For Fourier-based shift estimation, results were in agreement with the findings from the first series of experiments. More importantly, the second experimental setup allowed to assess the variability of error measurements for deconvolution results with identical method and parameters dependent on the displacement. Although we have not fully eliminated that variability, we reduced it to a similar extent as the method from [20], but at less computational effort.

Since insensitivity to random shifts is crucial for the reliability of the method as quality measurement for actual blind deconvolution results, the experiments presented in this paper mark a step closer to a fair quality measure for blind deconvolution.

Future work will be directed at continued refinement of our combined shift estimation and compensation approach. In the further course, it will be used for systematic state of the art blind deconvolution methods.

REFERENCES

[1] M. S. C. Almeida and L. B. Almeida, "Blind and semi-blind deblurring of natural images," IEEE Transactions on Image Processing, vol. 19, no. 1, pp. 36–52, 2010.

[2] L. Bar, N. Sochen, and N. Kiryati, "Variational pairing of image segmentation and blind restoration," in Computer Vision – ECCV2004, Part II, ser. Lecture Notes in Computer Science, T. Pajdla and J. Matas, Eds. Berlin: Springer, 2004, vol. 3022, pp. 166–177.

[3] T. F. Chan and C. K. Wong, "Total variation blind deconvolution," IEEE Transactions on Image Processing, vol. 7, pp. 370–375, 1998.

[4] T. F. Chan, A. M. Yip, and F. E. Park, "Simultaneous total variation image inpainting and blind deconvolution," International Journal of Imaging Systems and Technology, vol. 15, no. 1, pp. 92–102, 2005.

[5] R. Fergus, B. Singh, A. Hertzmann, S. T. Roweis, and W. T. Freeman, "Removing camera shake from a single photograph," in Proc. SIGGRAPH 2006, New York, NY, July 2006, pp. 787–794.

[6] V. Katkovnik, D. Paliy, K. Egiazarian, and J. Astola, "Frequency domain blind deconvolution in multiframe imaging using anisotropic spatially-adaptive denoising," in 14th European Signal Processing Conference (EUSIPCO 2006). Florence, Italy: EURASIP, Sep 4–8, 2006, pp. 1–5.

[7] R. Köhler, M. Hirsch, B. Mohler, B. Schölkopf, and S. Harmeling, "Recording and playback of camera shake: Benchmarking blind deconvolution with a real-world database," in Computer Vision – ECCV 2012, Part VII, ser. Lecture Notes in Computer Science, A. Fitzgibbon, S. Lazebnik, P. Perona, Y. Sato, and C. Schmid, Eds. Berlin: Springer, 2012, vol. 7578, pp. 27–40.

[8] A. Levin, Y. Weiss, F. Durand, and W. T. Freeman, "Understanding and evaluating blind deconvolution algorithms," in IEEE Conference on Computer Vision and Pattern Recognition, 2009, pp. 1964–1971.

[9] ——, "Efficient marginal likelihood optimization in blind deconvolution," in IEEE Conference on Computer Vision and Pattern Recognition, 2011, pp. 2657–2664.

[10] D. Li, R. M. Mersereau, and S. Simske, "Blind image deconvolution through support vector regression," IEEE Transactions on Neural Networks, vol. 18, no. 3, pp. 931–935, 2007.

[11] G. Liu, S. Chang, and Y. Ma, "Blind image deblurring using spectral properties of convolution operators," IEEE Transactions on Image Processing, vol. 23, no. 12, pp. 5047–5056, 2014.

[12] L. B. Lucy, "An iterative technique for the rectification of observed distributions," The Astronomical Journal, vol. 79, no. 6, pp. 745–754, 1974.

[13] P. Moser and M. Welk, "Robust blind deconvolution using convolution spectra of images," in 1st OAGM-ARW Joint Workshop: Vision Meets Robotics, K. Niel, P. M. Roth, and M. Vincze, Eds. Wels, Austria: Österreichische Computer-Gesellschaft, 2016, pp. 69–78.

[14] K. Panfilova and S. Umnyashkin, "Correlation-based quality measure for blind deconvolution restoration of blurred images based on Lucy-Richardson method," in IEEE Conference of Russian Young Researchers in Electrical and Electronic Engineering (ElConRus), 2019, pp. 2222–2225.

[15] W. H. Richardson, "Bayesian-based iterative method of image restoration," Journal of the Optical Society of America, vol. 62, no. 6, pp. 55–59, 1972.

[16] K. Schelten, S. Nowozin, J. Jancsary, C. Rother, and S. Roth, "Interleaved regression tree field cascades for blind image deconvolution," in IEEE Winter Conference on Applications of Computer Vision, 2015, pp. 494–501.

[17] C. R. Vogel and M. E. Oman, "Fast, robust total variation-based reconstruction of noisy, blurred images," IEEE Transactions on Image Processing, vol. 7, pp. 813–824, 1998.

[18] Z. Wang, A. C. Bovik, H. R. Sheikh, and E. P. Simoncelli, "Image quality assessment: From error visibility to structural similarity," IEEE Transactions on Image Processing, vol. 13, no. 4, pp. 600–612, 2004.

[19] M. Welk, "A robust variational model for positive image deconvolution," Signal, Image and Video Processing, vol. 10, no. 2, pp. 369–378, 2016

[20] M. Welk. "Superresolution alignment with innocence assumption: towards a fair quality measurement for blind deconvolution," in OAGM-ARW Joint Workshop: Vision, Automation and Robotics, P. M. Roth, M. Vincze, W. Kubinger, A. Müller, B. Blaschitz, and S. Stolc, Eds. Vienna, Austria: Verlag der Technischen Universität Graz, 2017, pp. 145–150.

[21] L. Xu, S. Zheng, and J. Jia, "Unnatural L_0 sparse representation for natural image deblurring," in IEEE Conference on Computer Vision and Pattern Recognition, 2013, pp. 1107–1114.

[22] Y.-L. You and M. Kaveh, "Anisotropic blind image restoration," in Proc. 1996 IEEE International Conference on Image Processing, vol. 2, Lausanne, Switzerland, Sept. 1996, pp. 461–464.